PHYSICAL REVIEW E **99**, 012902 (2019)

Magnus effect in granular media

Sonu Kumar, Manish Dhiman, and K. Anki Reddy[*]
Department of Chemical Engineering, Indian Institute of Technology, Guwahati 781039, Assam, India

(Received 6 June 2018; published 14 January 2019)

A spinning ball moving through air experiences a net lift due to the “Magnus effect” resulting from the pressure difference across its two sides. In this work, with the help of numerical simulations, we present a similar phenomenon on a circular intruder undergoing both translational and rotational motion in a two-dimensional granular medium. The direction of this “Magnus” lift in a granular medium, irrespective of its area fraction, is opposite to the general direction in viscous fluids in the range of velocities studied. We relate this effect to the switching in the direction of tangential forces, uneven shearing of the force chains, and uneven distribution in the number of contacts across the rotating intruder. Moreover, this is observed for area fractions Φ as low as 0.35 to as high as 0.82, which lies just below the jamming point. Distribution of the contact force around the intruder surface is also studied with respect to the nondimensionalized rotation speed of the intruder. A saturation in the lift to drag ratio is achieved at very high rotation speed, and the ratio is seen to be weakly dependent on the area fraction of the granular medium. The change in local flow fields of velocity, area fraction, and granular temperature around the intruder for several spin ratios is also discussed. The downstream wake of the intruder also deflects in the opposite direction when compared to the case in viscous fluids.

DOI: 10.1103/PhysRevE.99.012902

I. INTRODUCTION

Granular media, i.e., collections of discrete particles, exhibit different behaviors depending on their density. A few striking similarities have been found between the flowing granular medium and a viscous fluid. For example, many instabilities observed in viscous fluids are also observed in granular media, such as Kelvin-Helmholtz [1], Rayleigh-Plateau [2], Rayleigh-Taylor [3], etc. The capillary action that occurs due to cohesive and adhesive forces in fluids is also observed in a dry granular medium in which the forces of adhesion or cohesion are absent [4]. Despite these similarities, there exist many phenomena that are unique to granular media, such as jamming or Reynolds’ dilation. For example, the jamming of particles is a phenomenon [5] observed in granular media; however, the introduction of a helical inner wall texture prevents jamming of particles in vertical pipe flow [6], which illustrates the complex behavior of granular materials. The dynamics of objects immersed in fluids [7–10] has received a lot of attention over the past few decades. A solid object moving through a fluid experiences forces in a direction both perpendicular and parallel to the flow, namely lift and drag forces, respectively. An understanding of these forces has enabled massive developments in automobiles [11], ballistics [12], aircraft [13], satellites [14], etc. In granular media as well, a solid object when dragged experiences these two forces [15–19], and their proper understanding might give some insights about animal locomotion, drilling, and other applications.

When a rotating object moves through a fluid at a finite speed, it experiences a net lift force due to the pressure difference generated across the intruder from the rotation, and this is called the Magnus effect [20]. The direction of this lift force is along $\boldsymbol{\omega} \times \boldsymbol{V}$, where $\boldsymbol{\omega}$ and $\boldsymbol{V}$ are the angular velocity and translational velocity of the object relative to the stream. However, before Magnus, this had already been observed by both Newton [21] and Robins [22]. While addressing his earlier doubt about whether rays of light traveled in a curved path inside a prism, Newton [21] started a discussion on the deflection of a tennis ball flying in a curved path when hit by an oblique racket. He mentioned that the part of the ball where motion is greater must beat the air more violently than the part where the motion is less, and thus incite a greater reaction from the air generating this lift. Robins, via his experiment [22], also demonstrated the Magnus effect on spheres before Magnus himself. Euler, however, opposed Robins’s experimental demonstration and believed that this lift is generated due to “not so perfect” spheres trying to attain perfection [23].

When an intruder is rotated and translated at the same time inside the fluid, the surrounding fluid moves at different velocities and thus creates a pressure difference across the object, as per the classical Bernoulli principle. This pressure difference leads to a net lift force. Rayleigh [24], although agreeing with the pressure distribution, noted a weak step of this argument as this is applicable only for frictionless fluid since it did not account for the friction between the fluid and the cylinder’s surface due to the lack of a mathematical model to account for friction. Then, Lafay [25] showed, through his experiments on rotating cylinders, the distribution of pressure and the deflection of streamlines near the cylinder. Further, Thom [26–31] showed the effect of the Reynolds number, surface conditions, and a few other parameters, and he also calculated the drag, lift, and torque coefficients from his study. In 1904, Prandtl proposed the boundary layer theory

---

[*] anki.reddy@iitg.ac.in

2470-0045/2019/99(1)/012902(9)

in fluids [32]. Swanson in his study [12] used this boundary layer theory to explain the circulation around the cylinder. He suggested that the upper and lower boundary layers separate differently due to different velocities, and thus circulation is produced due to this behavior. With this, the origin of the Magnus force that took friction into account was proposed, and hence its direction was also justified.

However, there have been instances in which the direction of the Magnus effect is opposite, such as in free molecular flow [33,34] or in fluid flow at some specific Reynolds number [35]. The inverse Magnus effect observed at some of the Reynolds numbers is because the boundary layer that is moving against the surface (advancing side) of the sphere transitions to turbulent while the one that is moving with the surface (retreating side) does not [35], and hence the flow separates farther downstream. For the free molecular flow, a simple explanation is given with the probability theory and the change in momentum [34]. However, an intuitive answer for the inverse Magnus effect in such a system has been given by Borg *et al.* [33]. This inverse effect vanishes once the density of the molecular system exceeds a critical value.

In the present work, we investigate the Magnus effect in a granular medium with a rotating and translating intruder for dilute and dense regimes. Recent computational and experimental studies have shown that the lift generated in a granular medium can be due to the asymmetry caused by either the gravity [36] or the intruder shape [37] or the difference in the dilation and shear rate across the intruder [38]. A symmetric intruder that translates without any rotation will not experience any net lift. However, when rotational motion is there, it can experience a net lift force as observed in the present study. The generation of lift is still a significant challenge for an object moving through a granular medium. Understanding the forces on a translating and rotating intruder may provide insights about creating lift in an alternative way rather than by the wiggling of the intruder [39,40], and in projectile impact studies [41] by considering the effect of the rotation of the cannonball before a collision. In the present study, we also report similarities and differences of the Magnus effect in a granular medium versus viscous fluid.

II. SIMULATION METHODOLOGY

In this work, we employ the discrete element method (DEM) [42] to understand the Magnus effect in a two-dimensional granular medium. We consider a system of size $300d \times 200d$ along the x and y axes, respectively, where $d = 0.02$ m is the mean diameter of the granular particles. An intruder of diameter $d_{\text{intr}} = 5d$ is kept at the center (taken as the origin) of the simulation box spanning from $-150d$ to $150d$ along x and $-100d$ to $100d$ along y. While two frozen walls made up of disks of diameter d that are kept at $y = -99.5d$ and $99.5d$ confine the system along the y direction, the x direction is kept periodic. The simulation box is filled randomly with disks of mean diameter d with a polydispersity of 10%. The number of these particles in the system varies from 26 000 to 62 000 depending upon the area fraction Φ. The mass-area density of all particles is set to 20 kg/m^2 and the moment of inertia is set to that of a disk. For lower area fractions $\Phi < 0.5$, the initial configuration is generated by creating particles randomly in space. However, for higher $\Phi > 0.78$, the confining walls are kept far away initially, between which the desired number of particles are randomly created in space. Then, the confining walls are moved slowly to reach the size of the simulation system and thus to achieve the required Φ after the particles have almost zero kinetic energy. To achieve Φ in the intermediate range ($0.5 \leqslant \Phi \leqslant 0.75$), we first create a system of $\Phi = 0.78$ in random packing as per the scheme mentioned above, and then we remove the extra number of particles from the system selected randomly to achieve the desired Φ. There is no gravity in the system, and $\hat{\boldsymbol{z}}$ refers to the vector product $\hat{\boldsymbol{x}} \times \hat{\boldsymbol{y}}$. Figure 1 shows a simulation snapshot for $\Phi = 0.352$. We provided simulation movies in the Supplemental Material [43].

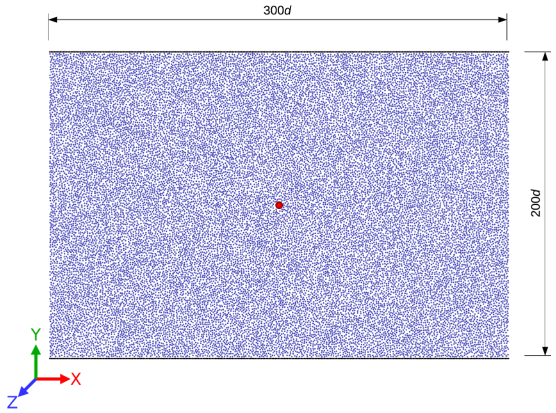

FIG. 1. The initial configuration for $\Phi = 0.352$. The red disk at the center shows the intruder of diameter d_{intr} located at the origin surrounded by granular particles (light blue particles) of mean diameter d. The two confining walls are located at $-99.5d$ to $99.5d$ (black particles).

In DEM we need to integrate the equations of motion to update the positions and velocities of particles as a function of time. Let us consider two particles i and j in contact having masses m_i and m_j, respectively, and diameters d_i and d_j, respectively. The force on i due to contact with j can be computed as [44]

$$\boldsymbol{F}^{\boldsymbol{n}}_{\boldsymbol{ij}} = \sqrt{\frac{d_i d_j}{2(d_i + d_j)}}\sqrt{\delta_{ij}}\left(K_n \delta_{ij}\hat{\boldsymbol{n}}_{\boldsymbol{ij}} - m_{\text{eff}}\gamma_n \boldsymbol{v}^{\boldsymbol{n}}_{\boldsymbol{ij}}\right), \quad (1)$$

$$\boldsymbol{F}^{\boldsymbol{t}}_{\boldsymbol{ij}} = -\sqrt{\frac{d_i d_j}{2(d_i + d_j)}}\sqrt{\delta_{ij}}\left(K_t \boldsymbol{\Delta s}_{\boldsymbol{ij}} + m_{\text{eff}}\gamma_t \boldsymbol{v}^{\boldsymbol{t}}_{\boldsymbol{ij}}\right), \quad (2)$$

where $\boldsymbol{F}^{\boldsymbol{n}}_{\boldsymbol{ij}}$ and $\boldsymbol{F}^{\boldsymbol{t}}_{\boldsymbol{ij}}$ are the normal and tangential contact forces. We restrict the upper limit of the magnitude of $\boldsymbol{F}^{\boldsymbol{t}}_{\boldsymbol{ij}}$ to $\mu|\boldsymbol{F}^{\boldsymbol{n}}_{\boldsymbol{ij}}|$, where μ is the coefficient of friction. In the force expressions, K_n and K_t are normal and tangential nonlinear spring constants, γ_n and γ_t are damping constants, $\hat{\boldsymbol{n}}_{\boldsymbol{ij}}$ is the unit vector along the line connecting the centers of particles i and j, m_{eff} stands for the effective mass, and δ_{ij} is the overlap between two particles. $\boldsymbol{\Delta s}_{\boldsymbol{ij}}$ stands for the tangential displacement vector between the two particles (truncated upon slipping criteria [44]), and the normal and tangential relative velocities are represented as $\boldsymbol{v}^{\boldsymbol{n}}_{\boldsymbol{ij}}$ and $\boldsymbol{v}^{\boldsymbol{t}}_{\boldsymbol{ij}}$, respectively. The force model adopted is in accordance with the variation in the

TABLE I. The values of the simulation parameters.

Parameters	Value
K_n	2 GPa
K_t	2.45 GPa
γ_n	8×10^6 (m s)$^{-1}$
γ_t	8×10^6 (m s)$^{-1}$
μ	0.5 (unless stated otherwise)
ρ (mass/area)	20 kg/m^2

coefficient of restitution with velocity [17,45]. We provided the simulation parameters in Table I.

The angular velocities of the particles are then updated according to the torque acting on it. The intruder is given a translational velocity of $\boldsymbol{V} = V_0\hat{\boldsymbol{x}} + 0\hat{\boldsymbol{y}}$ and a rotational velocity of $\boldsymbol{\omega} = \omega_0\hat{z}$ at time $t = 0$, where $\hat{x}$, $\hat{y}$, and $\hat{z}$ are the unit vectors along x, y, and z directions, respectively. The intruder moves at this constant translational and rotational velocity throughout the simulation. The simulation is carried out for the time it takes the intruder to travel one simulation box length along x. We have chosen a time step of 2×10^{-6} s. The simulation system is large enough for the forces on the intruder to be influenced by the periodic boundaries or the walls. In fact, taking a system three times as large as the current system does not alter the force on the intruder. The intruder achieves a mean "steady"-state behavior after a certain time, which is roughly the time it takes for the intruder to travel $30d$. Therefore, we calculate the averaged values of forces on an intruder by averaging the instantaneous values of forces over the time it takes the intruder to travel $270d$ after steady-state behavior has developed. We used a large-scale atomic/molecular massively parallel simulator (LAMMPS) [46,47] for our simulations. Ovito [48] and VMD [49] are used for postsimulation visualization.

III. RESULTS AND DISCUSSION

A. Pure translation of the intruder

The intruder is first moved at $\omega_0 = 0$, i.e., no rotational velocity for various translational velocities V_0. At any instant, the intruder might have N contacts with its surrounding particles at a given time t. The force that acts on an intruder in a direction opposite to its motion is drag, $\boldsymbol{F_D}$, while the one that acts perpendicular to it is lift, $\boldsymbol{F_L}$. We observe that for any given velocity, the drag on the intruder fluctuates with time with a well-defined mean, which has been reported in other drag studies [16–18]. We can write $\boldsymbol{F_D} = (D + \tilde{D})\hat{\boldsymbol{F}}_{\boldsymbol{D}}$, where D is the time-averaged drag while $\tilde{D}$ is the fluctuation in drag and $\hat{\boldsymbol{F}}_{\boldsymbol{D}}$ is a unit vector parallel to $-\boldsymbol{V}$. For zero rotational velocity, the time-averaged lift force acting on the intruder is zero. In a similar fashion, the number of contacts that the intruder has with surrounding particles at a given time t, $N(t)$, varies as $N(t) = N + \tilde{N}$, where N is the time-averaged number of contacts while $\tilde{N}$ refers to the fluctuation. We calculate D and N by averaging the instantaneous values over the time it takes the intruder to travel $270d$ after mean steady-state behavior has developed. These mean values are shown in Fig. 2. The mean drag D on the intruder in a two-dimensional system has been studied by Takehara *et al.* [50] for high area fraction Φ, and they proposed a relation between mean drag and intruder velocity as

$$D = D_0(\Phi) + \alpha(\Phi)V_0^2, \tag{3}$$

where $D_0(\Phi)$ and $\alpha(\Phi)$ are constants for a given Φ. Figure 2(a) shows that the mean drag follows a quadratic trend [$D_0(\Phi) \approx 0$] with a V_0^2 dependence in the range of Φ and V_0 explored. Figure 2(b) shows the average intruder contacts versus velocity. Although N varies linearly with V_0 at a lower Φ, it starts to deviate from the linear trend as Φ is increased. The mean drag D and the mean number of contacts are directly related. Generally, if force per contact remains constant, a higher N would imply higher D and vice versa. The relation between D and N in the present work is not necessarily linear. Apart from the number of contacts, it is also necessary that we analyze the distribution of contacts around the surface of the intruder.

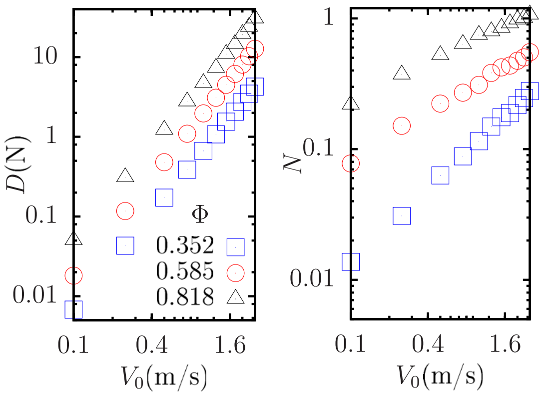

(a) (b)

FIG. 2. (a) Variation of D with V_0 for various Φ on a log-log plot. A linear fit gives a slope of roughly 2 suggesting quadratic dependence of the form $D \propto V_0^2$. (b) Variation of N with V_0 for various Φ. The symbols mean the same as in (a).

B. Combined translation and rotation of the intruder

In the next set of simulations, an angular velocity ω_0 along with the translational velocity V_0 is provided. In fluids, it is observed that the lift points in the direction of $\boldsymbol{\omega}\times\boldsymbol{V}$. However, in a granular medium, it is observed that the lift is in a direction $-\boldsymbol{\omega}\times\boldsymbol{V}$, which is opposite to that in fluids. Another parameter, namely the intruder spin ratio

$$\Omega = \frac{\omega_0 R}{V_0}, \tag{4}$$

given as the ratio of the intruder's surface speed due to the rotation and its translation speed, is used to compare the results for various V_0. We can also express the lift force as the sum of its mean and fluctuation as $\boldsymbol{F_L} = (L + \tilde{L})\hat{\boldsymbol{F}}_{\boldsymbol{L}}$, where $\hat{\boldsymbol{F}}_{\boldsymbol{L}}$ is the unit vector pointing in the direction of $-\boldsymbol{\omega}\times\boldsymbol{V}$, while L and $\tilde{L}$ are the mean and fluctuation in lift. Figure 3 shows the variation in the ratio of mean lift and mean drag versus Ω for various intruder speeds V_0. It can be seen that at $\Omega \approx 0$, this ratio has a value of zero because of the symmetry arguments. However, at a relatively high Ω, this ratio saturates to give

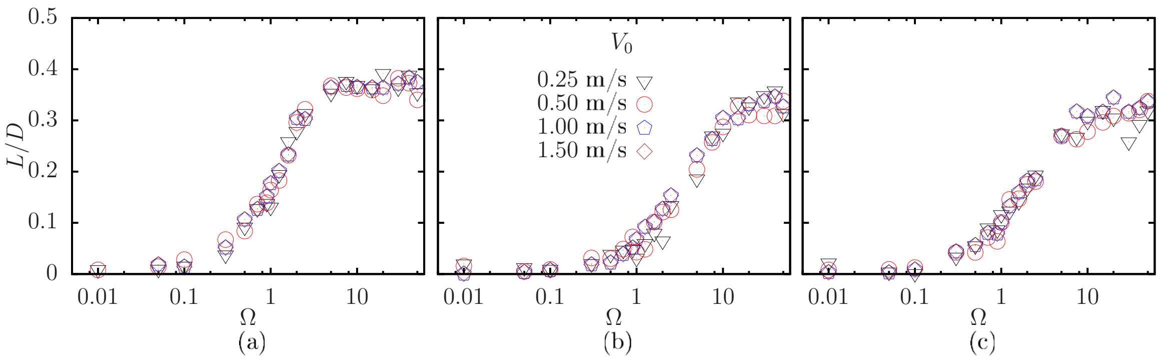

FIG. 3. The lift to drag ratio L/D against spin ratio ($\Omega = \omega_0 R/V_0$) for various V_0 for $\Phi =$ (a) 0.352, (b) 0.585, and (c) 0.818. The symbols mean the same as in (b).

almost a constant value of L/D. Moreover, the crossover from zero to this constant value seems to be occurring gradually with Ω but is most dominant at $\Omega \approx 1$, i.e., the maximum of $\partial(L/D)/\partial(\Omega)$ appears to be in the vicinity of $\Omega \approx 1$.

C. Origin of the Magnus force: Force distribution along the surface of the intruder

Let a point P be situated at an inclination of θ on the intruder's surface from the intruder's center with respect to the velocity vector $\boldsymbol{V}$. This point P moves at a given velocity if both translational and rotational components are added with each such unique point moving at a velocity of its own. The tangential velocity at such a point (assuming rotation is in a counterclockwise direction) is given as $V_{t,P} = \omega_0 R - V_0 \sin\theta$ while the normal velocity component is $V_{n,P} = V_0 \cos\theta$. If written in terms of Ω, $V_{t,P} = V_0(\Omega - \sin\theta)$. This would imply that for $\Omega \geqslant 1$, tangential velocity is always positive irrespective of θ, with the complete change in sign happening at $\Omega = 1$ because the maximum of the second term ($\sin\theta$) is 1, and hence $\Omega \geqslant 1$ would imply $V_{t,P} \geqslant 0$. Moreover, for an intruder moving in granular media, most of the contacts are situated on the front side of the intruder, and the wake region has close to zero contacts. A rather simplistic argument that can be given is that the tangential force or the frictional force acts in a direction opposite to the relative motion between the surfaces. If the intruder collides with another particle, say at rest, then the tangential force acts in a direction opposite to $V_{t,P}$, and since the majority of the contacts are between the range of $-\pi/2 \leqslant \theta \leqslant \pi/2$, the summation of these tangential forces has a component pointing in the $-\hat{\boldsymbol{y}}$ direction. This direction is opposite to $\boldsymbol{\omega} \times \boldsymbol{V}$, which is the direction of observed Magnus lift in fluids. This is the explanation for the inverse Magnus effect in the granular medium. This has been illustrated in Fig. 4 for the front side of the intruder, where the sum of the tangential forces leads to a net lift force. Additionally, it also shows that the majority of contacts with the intruder undergo slipping at high Ω, and the unidirectional behavior of the tangential force is well-developed at $\Omega = 1$. The above phenomenon exists for all area fractions Φ below the jamming point, as we find in our study for the range of velocities considered. Of course, at higher Φ, the phenomenon might be governed by other factors, such as a buckling of force chains, but the direction is nonetheless the same as that of the lower Φ system. In the case of the Magnus effect in free molecular flow, Borg *et al.* [33] suggested a critical density beyond which a transition occurs in the direction of the Magnus force. This does not occur in the case of the granular medium, since the sole reason for the Magnus force in free molecular flow is a preferential collision with the hemisphere facing the headwind. This occurs in the case of the granular medium, as we shall see later; however, the tangential forces are the major factor for the inverse Magnus effect, and thus switching in the direction of the Magnus force does not happen.

We also observe saturation in the value of L/D. In the present simulation model, the tangential contact force has an upper limit of μ times the normal contact force to account for slipping beyond this point. This saturation in the value of L/D is achieved when slipping starts for almost all the contacts, i.e., the ratio of the magnitude of the tangential and

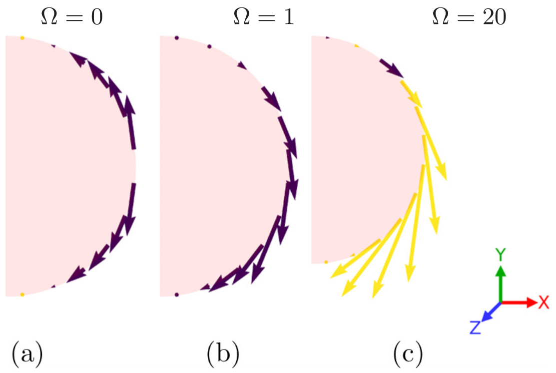

FIG. 4. The figure shows tangential force and its direction at a point on the surface of an intruder. Here the intruder is moving in the x direction and rotating in the counterclockwise direction. The front side of the intruder, which faces the majority of contacts, is depicted in this figure with vectors drawn along the surface of the intruder. The vectors are color-coded to suggest whether the contacts are undergoing slipping (yellow vectors) or not (violet vectors). The figure shows three cases of $\Omega =$ (a) 0, (b) 1, and (c) 20. When the spin ratio is zero, the sum of tangential forces cancels each other out in the y direction. However, as Ω is increased, a resultant vector is produced from the sum of these tangential forces. This resultant vector is the major cause for the Magnus effect in granular media.

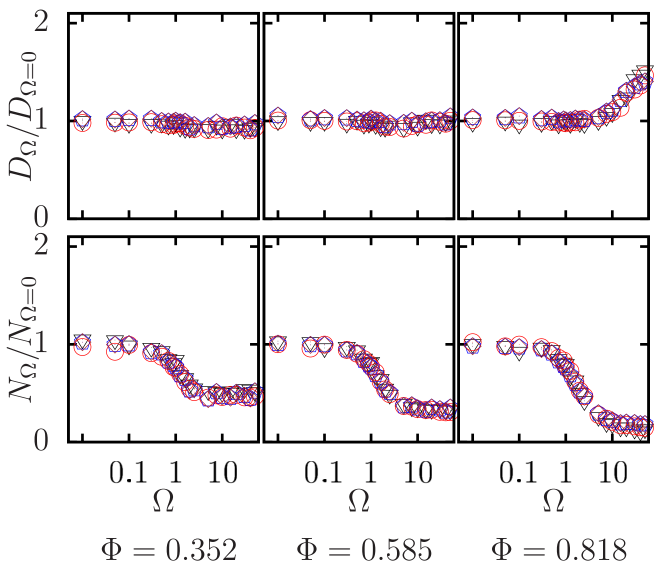

FIG. 5. Plot of D_Ω normalized by $D_{\Omega=0}$, which is the drag at a given spin ratio normalized by the case with zero spin ratio, against Ω (top row). Plot of $N_\Omega/N_{\Omega=0}$ vs Ω, where the former is the number of contacts at Ω normalized by N at $\Omega = 0$ (bottom row). The plots correspond to $\Phi = 0.352$, 0.585, and 0.818 from left to right. The symbols mean the same as in Fig. 3(b).

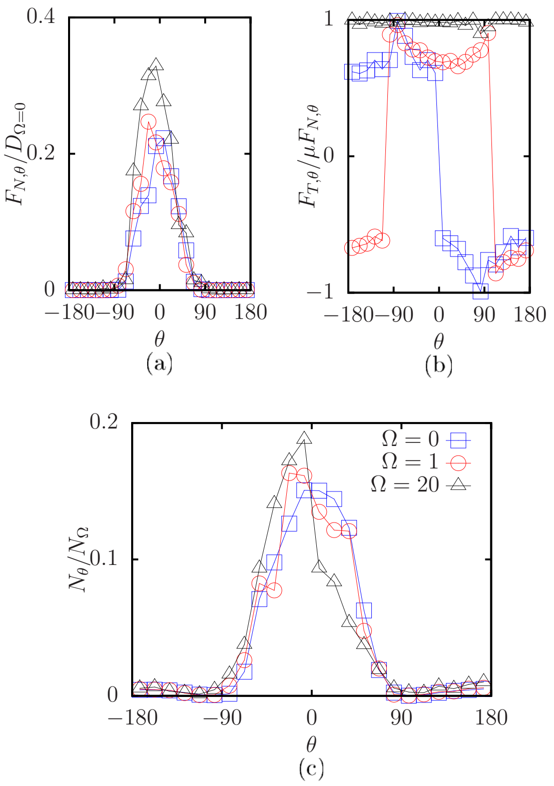

(a)

(b)

(c)

FIG. 6. (a) $F_{N,\theta}/D_{\Omega=0}$ vs θ, (b) $F_{T,\theta}/\mu F_{N,\theta}$ vs θ, and (c) N_θ/N_Ω vs θ for $\Phi = 0.818$. Please refer to (c) for the legends.

normal force becomes equal to the coefficient of friction, thus inducing slipping between the intruder and the particle for the majority of the contacts. We shall denote this saturation value as (L_∞/D_∞).

Figure 5 shows the variation of drag D_Ω and the number of contacts N_Ω at a given Ω normalized by the values at $\Omega = 0$. We find that the drag force remains almost constant for lower Φ while it increases after a constant regime for higher Φ. Moreover, the number of contacts is seen to decrease after a certain Ω for all Φ. This is an important observation, as the contribution to drag comes from the sum of force components opposite to the velocity vector of the intruder from all the contacts. When the number of contacts decreases, one might expect that the drag force decreases, too. However, that is true only if the force per contact remains the same. Therefore, it is important that we also study force per contact, together with how the distribution of contacts around the intruder varies with Ω. The only conclusion that can be drawn from this is that the force per contact increases with Ω. In the case of higher Φ, this increase is more significant.

Figure 6 shows the distribution of time-averaged quantities such as the total normal force $F_{N,\theta}$ normalized by $D_{\Omega=0}$, the total tangential force $F_{T,\theta}$ normalized by its maximum, $\mu F_{N,\theta}$, and the total number of contacts N_θ at P with a bin width of $\pi/12$ for $\Phi = 0.818$. $F_{N,\theta}/N_\theta$ represents the average normal force per contact and vice versa. Figure 6(c) shows how the contacts are distributed around the surface of the intruder. In the wake region of the intruder, i.e., $\theta \geqslant \pi/2$ and $\theta \leqslant -\pi/2$, the number of contacts is almost negligible, and hence the force contribution from the wake side is almost negligible. Therefore, our region of interest lies in $-\pi/2 < \theta < \pi/2$. We observe that in this region, the distribution of the number of contacts follows a trend with a peak at almost $\theta \approx 0$. It can be noticed that the symmetry of this distribution is broken as Ω is increased.

A value of $F_{T,\theta}/\mu F_{N,\theta} = 1$ implies slipping of the contact at that given point. Figure 6(b) justifies our previous discussion on the tangential force acting against the tangential velocity. It can also be observed that the change in direction of $F_{T,\theta}$ occurs for the majority of contacts at $\Omega = 1$ on the front side of the intruder $(-\pi/2 < \theta < \pi/2)$. Moreover, we find that at a higher value of Ω, the majority of the contacts start slipping, thus explaining that the proposed argument about saturation in L/D is correct. Although the number of contacts is decreasing in Fig. 5 for $\Phi = 0.818$, the drag force increases with the increase in Ω. This suggests that the normal contact force at a higher Φ seems to increase dramatically with Ω when compared to systems at a lower Φ. The reason can be the formation and breaking of the force chains while the intruder moves, something that is absent for a lower Φ. The normal force distribution $F_{N,\theta}$ remains almost symmetric about θ with the increase in spin ratio Ω.

D. Flow fields near the intruder

In this subsection, we show flow fields in the vicinity of the intruder, namely the velocity field with respect to the intruder $\langle V^* \rangle$, the area fraction field $\langle \Phi^* \rangle$, and the granular temperature field $\langle T_g^* \rangle$ in Fig. 7 for $\Omega = 0$, 1, and 10. The intruder is rotating in a clockwise direction for $\Omega > 0$ in the results of Fig. 7. Since the velocity field is plotted with respect to the intruder, the flow direction is from right to left. The

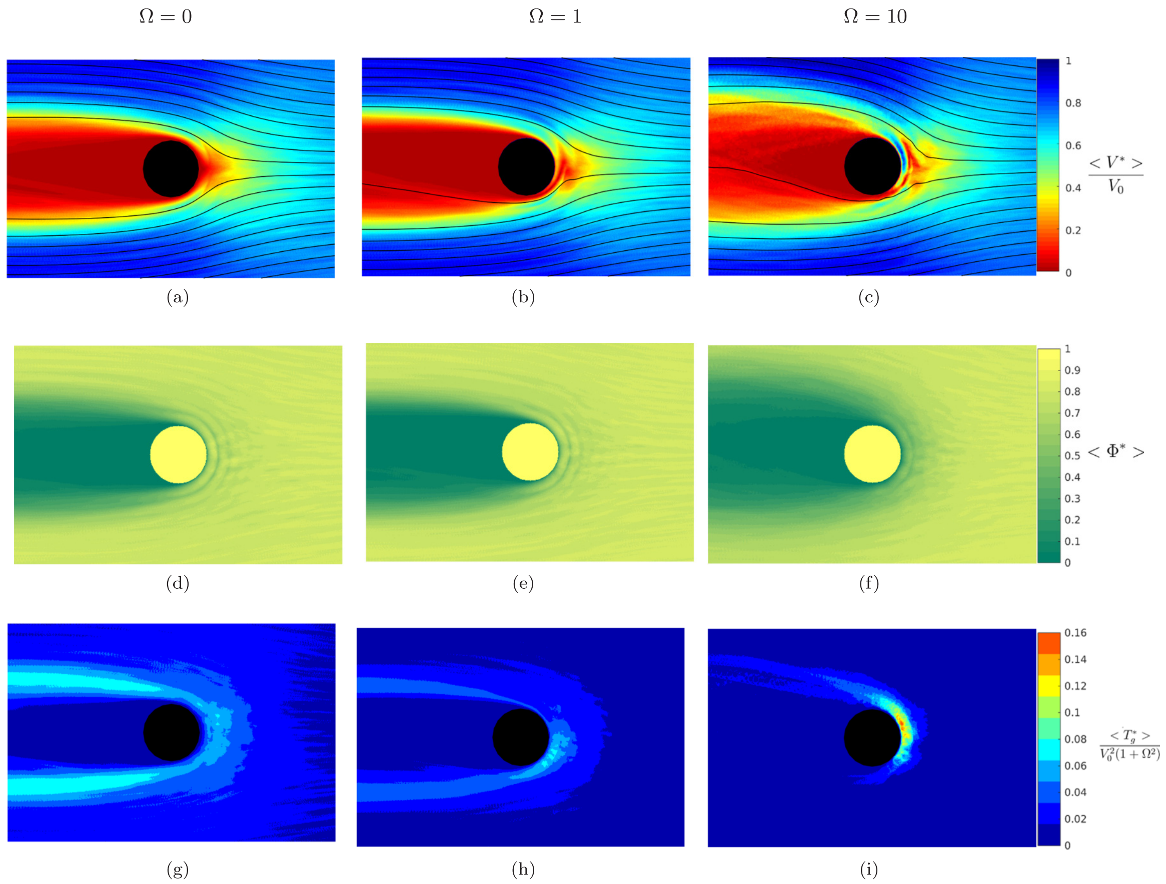

FIG. 7. The variation of normalized velocity field [(a), (b), and (c)], local area fraction [(d), (e), and (f)] and normalized local granular temperature [(g), (h), and (i)] in the vicinity of the intruder for $\Omega = 0$, 1, and 10, respectively. The black disk in the velocity and granular temperature fields represents the intruder while in the local area fraction plot it is represented by the yellow disk.

fields are calculated by averaging over 1000 configurations. The scheme used to calculate the flow fields is explained in detail in the Appendix.

Figures 7(a), 7(b) and 7(c) show the velocity field around the intruder for $\Omega = 0$, 1, and 10, respectively. The velocity field $\langle V^* \rangle$ is normalized by the magnitude of the intruder's translational velocity V_0. $\langle V^* \rangle$ is highly localized around the intruder. The streamlines are computed as the tangent to the velocity field at a given point. For $\Omega = 0$, the velocity field is symmetric about the line parallel to the flow direction and passing through the center of the disk. However, as Ω is increased, the flow field behaves asymmetrically about that line. We observe that the streamlines close to the retreating side of the intruder (the side whose surface moves against the flow) diverge in the upward direction while those over the advancing side are not deflected as much when compared to the nonrotational case $\Omega = 0$. This, in turn, represents the wake being pushed in the upward direction for $\Omega = 10$, suggesting a downward force on the intruder (or the direction $-\boldsymbol{\omega} \times \boldsymbol{V}$).

The distribution of the local area fraction $\langle \Phi^* \rangle$ is shown in Figs. 7(d), 7(e) and 7(f). We find that $\langle \Phi^* \rangle$ is very close to Φ (the area fraction of the system) except near the intruder or in its wake region. The wake is seen to widen with Ω, and typically there can be two distinct regions in the wake. The first region, which is the core of the wake, has $\langle \Phi^* \rangle \approx 0$ in the downstream of the intruder. In the second region of the wake, $\langle \Phi^* \rangle$ changes from 0 to Φ.

In Figs. 7(g), 7(h) and 7(i), we plot the granular temperature $\langle T_g^* \rangle$ (see the Appendix). We normalize $\langle T_g^* \rangle$ with the sum of the square of the translational and rotational velocity of the intruder, $V_0^2(1 + \Omega^2)$. The granular temperature is zero far away from the intruder. Moreover, it is also zero in the first region of the wake as there are hardly any particles ($\langle \Phi^* \rangle \approx 0$). However, the granular temperature varies in the region around the intruder and the second region of the wake as it is where the majority of the collisions can happen. We observe that the granular temperature reaches a maximum on the advancing side of the intruder for $\Omega = 10$. However, this maximum lies on the retreating side for $\Omega = 1$. The presence and location of this maximum warrant a future investigation.

IV. MODEL

The saturation value of the lift to drag ratio L_∞/D_∞ can be derived under some assumptions for the dilute systems with a simple model. Let us assume that $\Omega \gg 1$ and that Φ is in the dilute limit. We apply the following assumptions: (i) $F_{N,\theta}$ is symmetric with respect to θ. This is true as it should not vary much with Ω for very dilute systems. (ii) The contacts are undergoing slipping all the time (see Fig. 6). (iii) $F_{T,\theta}$ is always in a clockwise direction when an intruder is rotating

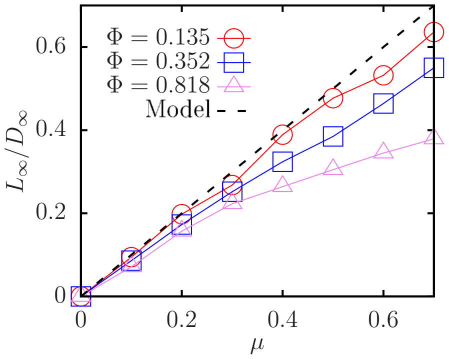

FIG. 8. L_∞/D_∞ vs μ for various Φ. The more dilute the system is, the closer the value of L_∞/D_∞ to the proposed model.

in a counterclockwise direction due to the fact that frictional forces act in a direction opposite to that of an intruder. Thus we can write

$$D_\infty = \sum (F_{N,\theta}\cos\theta - F_{T,\theta}\sin\theta). \tag{5}$$

Since $F_{T,\theta}$ is $\mu F_{N,\theta}$, which is symmetric about θ, we could simply write, based on our first assumption, $\sum \mu F_{N,\theta}\sin\theta = 0$, which would imply

$$D_\infty = \sum F_{N,\theta}\cos\theta. \tag{6}$$

Now,

$$L_\infty = \sum (F_{N,\theta}\sin\theta + F_{T,\theta}\cos\theta) \tag{7}$$

summed over all the contacts. Using the previous argument about the symmetry of $F_{N,\theta}$ about θ and $F_{T,\theta} = \mu F_{N,\theta}$, we could write

$$L_\infty = \sum \mu F_{N,\theta}\cos\theta = \mu \sum F_{N,\theta}\cos\theta = \mu D_\infty. \tag{8}$$

This would suggest

$$L_\infty/D_\infty = \mu, \tag{9}$$

which is almost valid in Fig. 8 for the dilute system ($\Phi = 0.135$). Moreover, for the frictionless case $\mu = 0$, the maximum lift to drag ratio is zero, thus suggesting no Magnus effect in the granular media of frictionless particles. We have plotted L_∞/D_∞ at various values of μ in Fig. 8 for various Φ. We observe that although L_∞/D_∞ follows a linear relationship with μ for low Φ, it deviates from $L_\infty/D_\infty = \mu$. The deviation of the predicted value from the real value is evident from the fact that the assumptions are approximate. The deviation increases with Φ.

If one were to write an expression for D_∞ and L_∞ without previous assumptions (except the fact that all contacts undergo slipping at high Ω, which is already seen in our results), we can write

$$D_\infty = \sum (F_{N,\theta}\cos\theta - \mu F_{N,\theta}\sin\theta), \tag{10}$$

$$L_\infty = \sum (F_{N,\theta}\sin\theta + \mu F_{N,\theta}\cos\theta), \tag{11}$$

$$\Rightarrow L_\infty = -\frac{D_\infty}{\mu} + \left(\mu + \frac{1}{\mu}\right)\sum F_{N,\theta}\cos\theta, \tag{12}$$

$$\Rightarrow \frac{L_\infty}{D_\infty} = -\frac{1}{\mu} + \left(\mu + \frac{1}{\mu}\right)\frac{\sum F_{N,\theta}\cos\theta}{D_\infty}. \tag{13}$$

When the intruder rotates in a counterclockwise direction, the retreating side of the disk ($-\pi/2 < \theta < 0$) experiences higher $F_{N,\theta}$ than the advancing side ($0 < \theta < \pi/2$). That means that the term $\sum F_{N,\theta}\sin\theta$ is negative for the counterclockwise rotation, implying that $D_\infty = \sum(F_{N,\theta}\cos\theta - \mu F_{N,\theta}\sin\theta) > \sum F_{N,\theta}\cos\theta$. Therefore, we write

$$\sum F_{N,\theta}\cos\theta = \kappa D_\infty, \tag{14}$$

where $0 < \kappa \leqslant 1$. We get

$$\frac{L_\infty}{D_\infty} = -\frac{1}{\mu} + \left(\mu + \frac{1}{\mu}\right)\kappa = \kappa\mu - (1-\kappa)\frac{1}{\mu} \tag{15}$$

$$\Rightarrow \frac{L_\infty}{D_\infty} < \mu. \tag{16}$$

Here κ accounts for the deviation of the symmetry of $F_{N,\theta}$ versus θ, which could be due to uneven shearing of force chains around the intruder. A value of $\kappa = 1$ implies perfect symmetry of $F_{N,\theta}$. The value of κ depends on the value of μ and Φ. For example, for dense systems $\Phi = 0.818$ and $\mu = 0.5$, $\kappa = 0.9$. However, for dilute systems $\Phi = 0.352$ and $\mu = 0.5$, $\kappa = 0.95$.

V. CONCLUSIONS AND FUTURE DIRECTIONS

In this article, we carried out computer simulations of an intruder with angular velocity $\boldsymbol{\omega}$ and translational velocity $\boldsymbol{V}$ in a granular medium, and we observed that it experiences the Magnus lift force. This lift force has a direction of $-\boldsymbol{\omega}\times\boldsymbol{V}$, which is opposite to the generally observed direction in fluids. We find that the tangential forces play a significant role in the generation of this Magnus lift. The change in the direction of relative motion between the grains and the intruder, induced as a consequence of its rotation, is what generates this lift. Moreover, we also analyzed the distribution of particles that are in contact with the intruder, and we noticed that the majority of the contacts undergo slipping after a specific spin ratio Ω leading to a saturation in the value of lift and drag ratio (L_∞/D_∞). We developed a simple mathematical model that could closely predict this (L_∞/D_∞) at least in the dilute regime. The case of rarefied gas systems also leads to an inverse Magnus effect, however the inverse lift switches direction once a critical density is exceeded. This is in sharp contrast to the case of the granular medium as the direction remains the same irrespective of the area fraction.

The intruder velocities considered in our study were in the inertial regime, i.e., a square dependence of drag force with V_0 was observed. An interesting future direction will involve velocities in the quasistatic regime. A mathematical basis either in the form of continuum modeling or incorporating the local rheology around the intruder can also help in understanding the Magnus effect in a granular medium. We also analyzed the local dynamics of particles around the intruder with the help of flow fields. This could be further explored to a more significant extent in the future. Additionally, the same study can be extended to a constant pressure system rather than the present constant volume system. A proper understanding of Magnus force in granular media may have implications in situations in which generating high amounts of lift to drag ratio is a significant challenge. Moreover, an extension of this study to a three-dimensional system in which the axis of rotation of an intruder and the velocity vectors are not necessarily perpendicular could be a future area of research.

ACKNOWLEDGMENT

We wish to acknowledge IITG for providing HPC facility, and we would like to thank Julian Talbot for his careful reading of our manuscript.

APPENDIX: FLOW-FIELD CALCULATION

In the main text, we have shown the variation in velocity field, area fraction, and the granular temperature near the intruder for various spin ratios at $V_0 = 0.25$ m/s and $\Phi = 0.818$. First, we have calculated the fields with a square bin of size $a_b = 0.05d$. We have added the effect of rotation and geometry of a granular particle while calculating these fields. Any particle that is moving might not necessarily have all the points on that particle moving at the same velocity. An example of this would be a car's tire while it is moving, i.e., the points on the tire not only move at different velocities but also in different directions. Hence, instead of averaging the magnitude of velocity at each bin based on the velocity of the center of the particle, we first average the v_x^* and v_y^* at each bin individually, which are the x and y components of velocity of the granular particle at that bin, respectively, with the contribution from the rotation velocity added. In obtaining the velocity field, we have used a slightly different method. In other works, such as Ref. [36], an averaging sphere of a certain radius is used to obtain the velocity field. However, this approach would not capture the velocity field near the intruder in great detail. In this work, we needed to calculate the area of a certain disk inside the bin that intersects a given averaging bin or completely submerges it inside itself. Of course, when it submerges, $A = a_b^2$, where A is the area of the disk inside the bin. However, when it does intersect the bin, it is tough to find the area analytically. Hence, in order to calculate that, certain assumptions are in the calculation of the area A. Consider a granular particle that is situated at position vector r_i (with a diameter d_i, x component of velocity as $v_{i,x}$, y component of velocity as $v_{i,y}$, and rotational velocity ω_i), and one of these bins has a position r_j^* and a horizontal and vertical velocity of v_x^* and v_y^*, respectively. We can write the angular orientation of the bin with respect to the ith disk's center and x axis as $\alpha = \cos^{-1}(\frac{r^*-r_i}{|r^*-r_i|}\cdot\hat{x})$. Therefore, if this bin lies inside the disk or intersects with it, then

$$v_x^* = v_{i,x} - \omega_i \sin\alpha |r_j^* - r_i| - V_0, \tag{A1}$$

$$v_y^* = v_{i,y} - \omega_i \cos\alpha |r_j^* - r_i|. \tag{A2}$$

And hence we write the mean velocity at a given bin relative to the intruder as

$$\langle v_x^* \rangle = \frac{\sum_{k=1}^{N_{\rm frames}} \sum_{j=1}^{N_{\rm mesh}} v_x^* \times \Gamma(r, r_j^*)}{\sum_{k=1}^{N_{\rm frames}} \sum_{j=1}^{N_{\rm mesh}} \Gamma(r, r_j^*)}, \tag{A3}$$

$$\langle v_y^* \rangle = \frac{\sum_{k=1}^{N_{\rm frames}} \sum_{j=1}^{N_{\rm mesh}} v_y^* \times \Gamma(r, r_j^*)}{\sum_{k=1}^{N_{\rm frames}} \sum_{j=1}^{N_{\rm mesh}} \Gamma(r, r_j^*)}. \tag{A4}$$

Here $\Gamma(r, r_j^*)$ is the area of the granular particles inside the bin if they overlap, and it is 0 otherwise. $\Gamma(r, r_j^*) = a_b^2$ when the bin is completely submerged inside the disk. In the case of intersection, we calculate $\Gamma(r, r_j^*)$ by diving the bin into several smaller bins of size $0.1a_b$, i.e., 100 smaller bins. Then we calculate the number of these subbins whose center lies inside the disk. We then express $\Gamma(r, r_j^*)$ as the sum of the area of these smaller bins. $N_{\rm frames} = 1000$ is the total number of simulation snapshots. In total, 1200 simulation snapshots were taken, but the first 200 frames are ignored in the calculation. We calculate the streamlines as the tangent to the velocity field at any given point. We also calculate the velocity field, the area fraction, and the granular temperature distribution around the intruder as

$$\langle V^* \rangle = \sqrt{\langle v_x^* \rangle^2 + \langle v_y^* \rangle^2}, \tag{A5}$$

$$\langle \Phi^* \rangle = \frac{\sum_{k=1}^{N_{\rm frames}} \sum_{j=1}^{N_{\rm mesh}} \Gamma(r, r_j^*)}{N_{\rm frames} a_b^2}, \tag{A6}$$

$$\langle T_g^* \rangle = \frac{\sum_{k=1}^{N_{\rm frames}} \sum_{j=1}^{N_{\rm mesh}} 0.5((v_x^* - \langle v_x^* \rangle)^2 + (v_y^* - \langle v_y^* \rangle)^2) \times \Gamma(r, r_j^*)}{\sum_{k=1}^{N_{\rm frames}} \sum_{j=1}^{N_{\rm mesh}} \Gamma(r, r_j^*)}. \tag{A7}$$

[1] D. J. Goldfarb, B. J. Glasser, and T. Shinbrot, Nature (London) **415**, 302 (2002).

[2] G. Prado, Y. Amarouchene, and H. Kellay, Phys. Rev. Lett. **106**, 198001 (2011).

[3] J. L. Vinningland, O. Johnsen, E. G. Flekkøy, R. Toussaint, and K. J. Måløy, Phys. Rev. Lett. **99**, 048001 (2007).

[4] F. Fan, E. J. R. Parteli, and T. Pöschel, Phys. Rev. Lett. **118**, 218001 (2017).

[5] A. V. K. Reddy, S. Kumar, K. A. Reddy, and J. Talbot, Phys. Rev. E **98**, 022904 (2018).

[6] F. Verbücheln, E. J. R. Parteli, and T. Pöschel, Soft Matter **11**, 4295 (2015).

[7] K. E. B. Lofquist and L. P. Purtell, J. Fluid Mech. **148**, 271 (1984).
[8] K. Miyazaki, D. Bedeaux, and J. B. Avalos, J. Fluid Mech. **296**, 373 (1995).
[9] A. J. Weisenborn, J. Fluid Mech. **153**, 215 (1985).
[10] S. K. Karanfilian and T. J. Kotas, J. Fluid Mech. **87**, 85 (1978).
[11] A. Huminic and G. Huminic, Int. J Automot. Technol. **18**, 397 (2017).
[12] W. Swanson, J. Basic Eng. **83**, 461 (1961).
[13] D. M. Bushnell, Proc. Inst. Mech. Eng., Pt. G: J. Aeros. Eng. **217**, 1 (2003).
[14] B. K. Ching, D. R. Hickman, and J. M. Straus, J. Geophys. Res. **82**, 1474 (1977).
[15] J. Geng and R. P. Behringer, Phys. Rev. E **71**, 011302 (2005).
[16] J. E. Hilton and A. Tordesillas, Phys. Rev. E **88**, 062203 (2013).
[17] S. Kumar, K. A. Reddy, S. Takada, and H. Hayakawa, arXiv:1712.09057.
[18] R. Albert, M. A. Pfeifer, A. L. Barabasi, and P. Schiffer, Phys. Rev. Lett. **82**, 205 (1999).
[19] R. Bharadwaj and C. Wassgren, Phys. Fluids **18**, 043301 (2006).
[20] G. Magnus, Ann. Phys. **164**, 1 (1853).
[21] I. Newton, Philos. Trans. R. Soc. London **5-6**, 3078 (1671-72).
[22] B. Robins, *New Principles of Gunnery*, edited by C. Hutton (F. Wingrave, London, 1805; originally published in 1742).
[23] L. Euler and H. Brown, *The True Principles of Gunnery (a translation by H. Brown)* (J. Nourse, London, 1777).
[24] L. Rayleigh, Mess. Math. **7**, 14 (1877).
[25] A. Lafay, Rev. Méc. **30**, 417 (1912).
[26] A. Thom, Ph.D. thesis, University of Glasgow, 1926.
[27] A. Thom, *Experiments on the Flow Past a Rotating Cylinder* (Aeronautical Research Committee, Reports and Memoranda, London, 1931), Vol. 1410.
[28] A. Thom, *Experiments on the Air Forces on Rotating Cylinder* (Aeronautical Research Committee, Reports and Memoranda, London, 1925), Vol. 1018.
[29] A. Thom and S. Sengupta, *Air Torque on a Cylinder Rotating in an Air Stream* (Aeronautical Research Committee, Reports and Memoranda, London, 1932), Vol. 1520.
[30] A. Thom, *Effect of Discs on the Air Forces on a Rotating Cylinder* (Aeronautical Research Committee, Reports and Memoranda, London, 1934), Vol. 1623.
[31] A. Thom, *The Pressures around a Cylinder Rotating in an Air Current* (Aeronautical Research Committee, Reports and Memoranda, London, 1926), Vol. 1082.
[32] L. Prandtl, in *Verhandlungen des dritten internationalen Mathematiker-Kongresses in Heidelberg 1904*, edited by A. Krazer (Teubner, Leipzig, Germany, 1905), p. 484.
[33] K. I. Borg, L. H. Söderholm, and H. Essén, Phys. Fluids **15**, 736 (2003).
[34] P. D. Weidman and A. Herczynski, Phys. Fluids **16**, L9 (2004).
[35] J. Kim, H. Choi, H. Park, and J. Y. Yoo, J. Fluid Mech. **754**, R2 (2014).
[36] F. Guillard, Y. Forterre, and O. Pouliquen, Phys. Fluids **26**, 043301 (2014).
[37] Y. Ding, N. Gravish, and D. I. Goldman, Phys. Rev. Lett. **106**, 028001 (2011).
[38] B. Debnath, K. K. Rao, and P. R. Nott, AIChE J. **63**, 5482 (2017).
[39] L. Huang, X. Ran, and R. Blumenfeld, Phys. Rev. E **94**, 062906 (2016).
[40] R. D. Maladen, Y. Ding, C. Li, and D. I. Goldman, Science **325**, 314 (2009).
[41] M. P. Ciamarra, A. H. Lara, A. T. Lee, D. I. Goldman, I. Vishik, and H. L. Swinney, Phys. Rev. Lett. **92**, 194301 (2004).
[42] P. A. Cundall and O. D. L. Strack, Géotechnique **29**, 47 (1979).
[43] See Supplemental Material at http://link.aps.org/supplemental/10.1103/PhysRevE.99.012902 for videos corresponding to the demonstration of the Magnus effect in a granular medium.
[44] N. V. Brilliantov, F. Spahn, J.-M. Hertzsch, and T. Pöschel, Phys. Rev. E **53**, 5382 (1996).
[45] T. Schwager and T. Poschel, Phys. Rev. E. **57**, 650 (1998).
[46] S. Plimpton, J. Comput. Phys. **117**, 1 (1995).
[47] S. Plimpton, P. Crozier, and A. Thompson, *LAMMPS-Large-Scale Atomic/Molecular Massively Parallel Simulator* (Sandia National Laboratories, 2007).
[48] A. Stukowski, Modell. Simul. Mater. Sci. Eng. **18**, 015012 (2010).
[49] W. Humphrey, A. Dalke, and K. Schulten, J. Mol. Graph. **14**, 33 (1996).
[50] Y. Takehara and K. Okumura, Phys. Rev. Lett. **112**, 148001 (2014).